Laser-controlled electronic symmetry breaking in a phenylene ethynylene dimer: Simulation by the hierarchical equations of motion and optimal control

Amine Jaouadi,[1] Joachim Galiana,[2] Etienne Mangaud,[3] Benjamin Lasorne,[2] Osman Atabek,[4,*] and Michèle Desouter-Lecomte[5,†]

[1]*Graduate School of Engineering, ECE Paris, 75015 Paris, France*
[2]*ICGM, Univ Montpellier, CNRS, ENSCM, Montpellier, France*
[3]*MSME, Université Gustave Eiffel, UPEC, CNRS, 77454 Marne-La-Vallée, France*
[4]*Institut des Sciences Moléculaires, Université Paris-Saclay, UMR8214, CNRS, 91400 Orsay, France*
[5]*Université Paris-Saclay, CNRS, Institut de Chimie Physique UMR8000, 91405 Orsay, France*

The ability to prepare a specific superposition of electronic excited states leading to a transitory symmetry breaking of the electronic density in complex systems remains a challenging concern. We investigate how an initial coherence can be controlled by laser fields. The selected molecular system is a symmetric dimer of phenylene ethynylene presenting different interesting properties: Two bright nearly degenerate excited states coupled through a conical intersection are addressable by orthogonal transition dipole moments and are well separated from neighboring states. Creating a superposed state with equal weights corresponds to a right or left electronic localization as in the double-well system followed by a transitory oscillation between the two wells. To ensure a spectral bandwidth typically smaller than 0.25 eV, the pulse duration is in the tens of femtoseconds range, so nuclear motion cannot be neglected. Optimal control theory (OCT) is applied with guess fields that effectively create the target coherence in the absence of dephasing due to the vibrational baths. We analyze the field reshaping proposed by the control and we further fit a sequence of pulses on the optimal field. The overall result is efficient and robust disymmetry control over reasonable timescales of few tens of femtoseconds, exceeding the pulse duration. The monotonically convergent algorithm is combined with the hierarchical equations of motion (HEOM) able to treat strongly coupled non-Markovian dynamics. We also check the implementation of the combined OCT-HEOM approach in the tensor-train representation with propagation using the time-dependent variational method.

I. INTRODUCTION

Controlling electron dynamics and quantum coherence to trigger particular nuclear displacements is the basic concern of the emerging fields of attophysics and femtochemistry [1–7]. The preparation by laser fields of specific superpositions of excited eigenstates generates an electron density reorganization or symmetry breaking [8,9] and the correlated directional properties of the nuclear motion.

The timescale of the light pulse fixes the spectral bandwidth and this could be prohibitive when the target is a narrow band of some particular bright excited states. To avoid interference with additional bright states, the pulse duration should not be less than a few tens of femtoseconds. It is then similar to some vibrational periods and electronic decoherence will occur during the interaction with the laser field. The variation of the off-diagonal elements of the reduced density matrix is due to relaxation induced here by the nonadiabatic transitions and to dephasing caused by the tuning of the energies. Developing strategies to improve the preparation of superposed electronic states and to preserve

coherence at least during the pulse remains a challenging objective in complex molecular systems [10–16]. Our goal concerns the timely issue of optimizing control procedures for quantum systems strongly coupled to structured environments and leading to non-Markovian reduced dynamics. This requires implementing an optimization procedure of the parametric space among numerous available methods [17–24] with an efficient treatment of non-Markovian open systems [16,25–27]. There are two main ways to account for the non-Markovianity, reviewed, for instance, in Ref. [28]. The dimension of the active system may be increased by including a reasonable number of discrete modes while the residual bath is weakly coupled and Markovian [29–37]. The other scenario simulates the baths by continuous spectral densities leading to time-local coupled hierarchical equations of motion (HEOM) [38–41]. In this work we combine HEOM with a monotonically convergent algorithm of optimal control theory (OCT) in the presence of dissipation [42]. For non-Markovian dissipation, the backward propagation to solve the equation with the final target condition requires special attention [43]. This is established at the second order [44] and generalized for HEOM [27]. We compare the approach using a standard Cash-Karp Runge-Kutta adaptive algorithm [45] with a tensor-train (TT) representation [37,46–52] recently implemented in HEOM [53–56].

---
*Deceased.
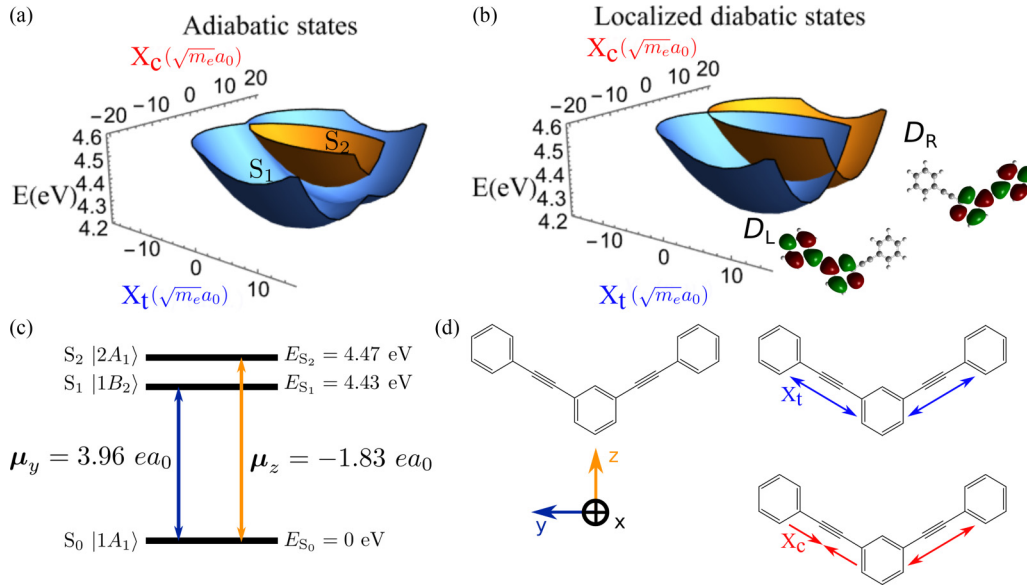†michele.desouter-lecomte@universite-paris-saclay.fr

FIG. 1. Three-dimensional schematic view of (a) the conical intersection between the adiabatic excited states S_1 and S_2 and (b) the corresponding localized diabatic states D_L and D_R with their corresponding electronic lowest unoccupied molecular orbitals [61,65]. Also shown are (c) *ab initio* energies and transition dipole moments at the minimum geometry of the ground state S_0 and (d) the *x*-, *y*-, and *z*-axis convention together with the main vibrational mode X_t of A_1 symmetry belonging to the tuning bath and the main antisymmetric coupling bath mode X_c of B_2 symmetry.

We consider a symmetric molecular system: a metasubstituted dimer of phenylene ethynylene of C_{2v} symmetry, which is a building block of treelike dendrimers [57–59]. The first excited manifold is composed of two quasidegenerate bright states (the gap at the Franck-Condon geometry is 0.044 eV) of different symmetry only radiatively coupled to the ground state. The two states are coupled through a conical intersection [60], characterized in Ref. [61]. The model is calibrated from molecular *ab initio* data in the framework of the linear vibronic coupling (LVC) model currently used to describe conical intersections [62]. The adiabatic excited states are delocalized over the whole nuclear skeleton. Our aim is to create a superposed excited state with a broken symmetry leading to a transitory localization on the left or right part of the molecule (see Fig. 1).

For the optimization, we first explore guess fields inspired by a simplified three-state V-type model without dissipation for which there is an analytical solution based on simultaneous $\pi/\sqrt{2}$ pulses with orthogonal polarization and equal duration [63]. In the second step we use OCT with an optimization on a time grid to offer the maximum flexibility to the pulse shape. The interpretation of the resulting reshaped optimized field actually suggests a sequence of a few pulses which can further be designed by shaping techniques. Still another way is to provide simple analytical forms for the individual pulses and fit their parameters with the optimized field.

The paper is organized as follows. In Sec. II we present the *ab initio* data and particularly the parameters of the LVC model of the conical intersection between the excited states. Section III describes the spectral densities of the tuning and coupling baths, paying particular attention to the correlation of the tuning baths. In Sec. IV we explicate the strategies for the field-driven dynamics. The results are given in Sec. V. All the equations for the OCT-HEOM approach are

summarized in Appendix A and the TT representation is given in Appendix B.

II. MODEL

The molecular system is a C_{2v} metasubstituted dimer of phenylene ethynylene. We focus on the first excited manifold with two bright excited states $S_1(1B_2)$ and $S_2(2A_1)$ coupled to the ground $S_0(1A_1)$ state only radiatively through corresponding transition dipoles. All calculations were performed with the GAUSSIAN16 package (revision A03) [64] using density-functional theory (ground state S_0) and time-dependent density-functional theory (excited states S_1 and S_2) at the CAM-B3LYP/6-31+G* level of theory, the validity of which having been assessed already in previous works [61,65]. The electronic-state symmetries, energies, and oscillator strengths at the S_0 minimum and S_2/S_1 minimum-energy conical intersection (MECI) geometries are provided in the Supplemental Material [66].

The molecule is planar and positioned according to Mulliken's axis convention for C_{2v} symmetry (as shown in Fig. 1). More precisely, z (A_1) is the C_2 rotation axis, y (B_2) lies within the molecular plane, and x (B_1) is orthogonal to it. The vertical energies and the dipole transition moments at the ground equilibrium geometry (minimum of S_0) are given in Fig. 1. The two excited states are coupled through a conical intersection that was recently characterized [61]. This induces an ultrafast nonadiabatic funneling between these states. We consider the A_1 and B_2 in-plane motions by discarding soft out-of-plane torsions, which are expected to play a secondary role. The S_1 and S_2 states may cross in C_{2v} symmetry. The S_1 state exhibits two equivalent minima in C_S geometry connected by B_2 deformations. A scheme of the adiabatic potential energy surfaces is given in Fig. 1. This adiabatic representation

may be described in terms of two interesting diabatic basis sets leading to the so-called delocalized or localized diabatic states, respectively [67]. The delocalized states are adapted to the A_1 or B_2 symmetries. They coincide with the adiabatic states along symmetry-conserving A_1 motions, which are the tuning modes making the energy gap fluctuate. They are coupled by a potential electronic coupling along B_2 modes, which are the coupling modes. In the LVC model, the two excited delocalized diabatic states are written in mass-weighted coordinates by choosing the Franck-Condon geometry as a reference point and by neglecting any Duschinsky rotation of the normal modes. Accordingly, the N normal modes q_j are the same in each electronic state; only their equilibrium position $q_{j,0}^{(m)}$ depends on the electronic state m. The N normal modes are separated in tuning and coupling classes $N = N_t + N_c$ according to their symmetry, the corresponding modes being denoted by $q_{j,t}$ or $q_{j,c}$ respectively. The Hamiltonian matrix in the delocalized diabatic basis set reads

$$H_{mm}^{\text{deloc}} = \varepsilon_{\text{FC}}^{(m)} + \frac{1}{2} \sum_j^N \left(p_j^2 + \omega_j^2 q_{j,t\,(c)}^2 \right) - \sum_j^{N_t} d_j^{(m)} q_{j,t}, \quad (1)$$

$$H_{mm'}^{\text{deloc}} = \sum_j^{N_c} c_j^{(mm')} q_{j,c}, \quad (2)$$

where $\varepsilon_{\text{FC}}^{(m)}$ is the energy at the Franck-Condon geometry. In the harmonic model, the gradients $d_j^{(m)} = \omega_j^2 q_{j,t,0}^{(m)}$ are related to the distance $q_{j,t,0}$ between the minimum position of the excited state and the reference point. Good agreement between the two values is a validation of the harmonic hypothesis. The gradients of the coupling are computed by a method detailed in Ref. [68]. The components of relevant shifts and gradients in terms of in-plane normal modes (A_1 and B_2) are listed in the Supplemental Material [66]. They lead to the definition of collective coordinates ensuring the whole coupling to the electronic system

$$X_t^{(m)} = \sum_j^{N_t} d_j^{(m)} q_{j,t} / D_{0t}^{(m)} \quad (3)$$

and

$$X_c^{(mm')} = \sum_j^{N_c} c_j^{(mm')} q_{j,c} / D_{0c}^{(mm')} \quad (4)$$

with $D_{0t}^{(m)} = \sum_j^{N_t} d_j^{(m)2}$ and $D_{0c}^{(mm')} = \sum_j^{N_c} c_j^{(mm')2}$. In Fig. 1 we illustrate the main vibrational tuning and coupling modes contributing to the effective coordinates. They are the high-frequency stretching modes of the two triple bonds connecting the phenyl rings with the symmetric A_1 deformation for $X_t^{(m)}$ and the antisymmetric B_2 one for $X_c^{(mm')}$, respectively.

By transforming the 2×2 subspace of the excited delocalized diabatic basis set by a $\pi/4$ rotation matrix, the equilibrium positions of the diabatic localized states D_L and D_R correspond to those of the adiabatic lowest state, which displays a double-well profile along a B_2 displacement. Each localized diabatic state corresponds to the localization of the excited electronic density on one side or the other of the dimer as illustrated in Fig. 1.

III. OPEN QUANTUM SYSTEM

According to the open quantum system approach, the full vibronic space is partitioned into an active subsystem explicitly treated quantum mechanically and its surroundings addressed as a bath. The choice of the partition is a key ingredient to get a computationally tractable master equation. Hierarchical equations of motion are one of the standard strategies to solve the system-bath dynamical equations in a numerically exact way provided the bath is harmonic and linearly coupled to the system. Different partitions have been used in HEOM applications with a conical intersection by including in the active system the main tuning and coupling modes and the corresponding potential energy surfaces coupled to residual baths [69], or only the electronic subsystem at a reference geometry (here the equilibrium geometry of the ground electronic state) [63,70,71], the baths being all the nuclear tuning or coupling vibrational modes at thermal equilibrium at the reference point. We adopt the second strategy. The full Hamiltonian is then rewritten as

$$H = H_S + H_{SB} + H_B, \quad (5)$$

where H_S is the diabatic, delocalized, symmetry adapted electronic Hamiltonian at the Franck-Condon geometry. At this reference point, the diabatic and adiabatic energies coincide and the coupling vanishes. The energies are given in Fig. 1. The transformation to the localized diabatic representation

$$H_S^{\text{loc}} = U^\dagger H_S U \quad (6)$$

involves the matrix

$$U = \begin{pmatrix} 1 & 0 & 0 \\ 0 & \frac{1}{\sqrt{2}} & -\frac{1}{\sqrt{2}} \\ 0 & \frac{1}{\sqrt{2}} & \frac{1}{\sqrt{2}} \end{pmatrix}. \quad (7)$$

The system-bath coupling is $H_{SB} = \sum_b S_b B_b$, where $b = t, c$ designates the bath, with S_b and B_b operators of the electronic and of the complementary vibrational spaces, respectively. The linear coupling is induced by the antisymmetric coupling modes, which are coupled off-diagonally by the operator $S_c = |S_1\rangle\langle S_2| + |S_2\rangle\langle S_1|$. The tuning baths inducing fluctuation of the energy gaps are often considered as independent when they gather modes belonging to different molecular sites embedded in complex structures as in light harvesting complexes. The operator relating each tuning bath is then the projector on the corresponding electronic state $S_{t,m} = |m\rangle\langle m|$ and the total contribution to the coupling term is $S_{t,m_1} B_{b_1} + S_{t,m_2} B_{b_2}$. In the case of the conical intersection in a single molecular system, the modes are assumed to be the same in the excited electronic states. When some modes lead to different gradients in the different states, they are correlated and make cross terms appear in the correlation function of the bath modes. An approximate way of accounting for bath correlation is to work with a single bath coupled via a composite operator $S_t = |m\rangle\langle m| + w|m'\rangle\langle m'|$. Limit values $w = 1$ and $w = -1$ correspond to fully correlated and anticorrelated baths, respectively, i.e., each mode leads to the same gradient or the opposite gradient in the two electronic states [72]. We take a model with a constant correlation factor fixed by the principal A_1 mode leading the largest gradient and we use the operator $S_t = |S_1\rangle\langle S_1| + 0.893|S_2\rangle\langle S_2|$ as discussed below
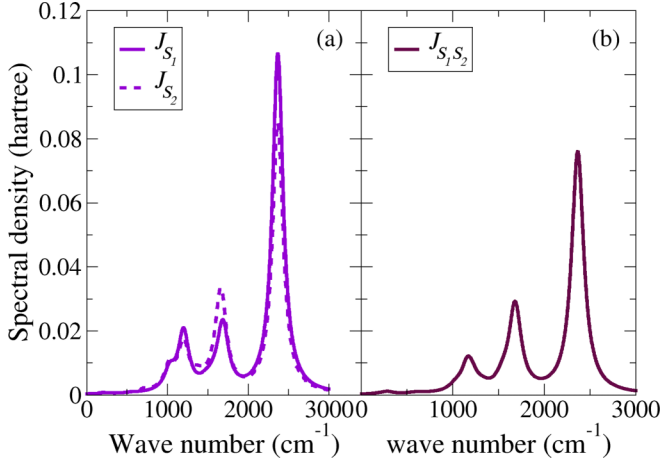
FIG. 2. Discrete spectral densities (8) broadened by a Lorentzian function with a width of wave number 160 cm^{-1}: (a) J_{S_1} and J_{S_2} of the tuning baths and (b) $J_{S_1 S_2}$ of the coupling bath.

when we present the bath spectral densities. A more sophisticated method introducing a frequency-dependent correction of the spectral density has been used recently [73].

The bath operators are collective modes having the dimension of energy. For the correlated tuning baths involving the composite operator S_t, we use the tuning collective mode $B_t = \sum_j^{N_t} d_j^{(S_1)} q_{j,t} = D_{0t}^{(S_1)} X_t^{(S_1)}$, where $d_j^{(S_1)}$ are the S_1 gradients at the reference point. The coupling collective mode is $B_c = \sum_j^{N_c} c_j^{(S_1 S_2)} q_{j,c} = D_{0c}^{(S_1 S_2)} X_c$, where $c_j^{(S_1 S_2)}$ are the gradients of the interstate coupling.

The key tool is the spectral density

$$J_{t\,(c)}(\omega) = \frac{\pi}{2} \sum_j f_j^2 \omega_j^{-1} \delta(\omega - \omega_j), \qquad (8)$$

where f_j^2 is the strength of the coupling at each frequency and $f_j = d_j$ or c_j for t or c, respectively. It is linked to the so-called thermal spectral density $J_{t\,(c)}^T(\omega) = J_{t\,(c)}(\omega)(e^{\beta\omega} - 1)^{-1}$ with $\beta = 1/k_B T$. The $J_{t\,(c)}^T(\omega)$ is used in different approaches with discrete modes to account for the temperature. In the continuous approach, the master equation involves the Fourier transform $C_{t\,(c)}(t) = \int_{-\infty}^{\infty} d\omega J_{t\,(c)}^T(\omega) e^{-i\omega t}$ that is the two-time correlation function of the collective modes $C_{t\,(c)}(t) = \langle B_{t\,(c)}(t) B_{t\,(c)}(0) \rangle_{\mathrm{eq}}$, where $B_{t\,(c)}(t)$ is the Heisenberg representation of the operator and $\langle \cdot \rangle_M$ denotes the average over a Boltzmann distribution at temperature T. The δ distribution of the discrete spectral density is broadened by a Lorentzian smoothing function $\delta(\omega - \omega_j) \rightarrow \frac{1}{\pi} \frac{\Gamma}{(\omega - \omega_j)^2 + \Gamma^2}$ [74–76]. In this work we use Γ with a wave number 160 cm^{-1}. The tuning spectral densities of the two excited states denoted by J_{S_1} and J_{S_2} are given in Fig. 2(a). Figure 2(b) displays the spectral density of the coupling bath $J_{S_1 S_2}$. The smooth spectral densities have been fitted by three two-pole Tannor-Meier Lorentzians [77]

$$\mathcal{J}_{t\,(c)}(\omega) = \sum_i^{N_{l,t\,(c)}} \frac{p_i \omega}{\left[(\omega + \Omega_i)^2 + \Gamma_i^2 \right] \left[(\omega - \Omega_i)^2 + \Gamma_i^2 \right]}, \qquad (9)$$

where $N_{l,t\,(c)}$ is the number of two-pole Lorentzians in the tuning or coupling bath. The fitted functions and their parameters are given in the Supplemental Material [66]. The main components are the high-frequency modes corresponding to the symmetric (wave number 2367.4 cm^{-1}) and antisymmetric (wave number 2366.5 cm^{-1}) stretches of the acethylenic bond (see Fig. 1). The central peaks at wave number 1692.1 cm^{-1} for the tuning modes and wave number 1681.9 cm^{-1} for the coupling ones are associated with A_1 or B_2 in-plane deformations of the central benzene ring. The third peak corresponds to secondary contributions to the tuning (A_1 at $1199c$ cm^{-1}) and to the coupling (B_2 at $1160c$ cm^{-1}) modes. They describe in-phase and out-of-phase stretches of the bonds linking the acetylenic moieties to the benzenic ones, respectively, with induced in-plane triangular distortions of the rings.

We assume a positive correlation between the S_1 and S_2 tuning baths independent of the frequency and fixed by the high-frequency modes with wave number 2367 cm^{-1}. This approximation seems reasonable and reduces the computational effort by introducing a single tuning bath and a composite system-bath operator.

The partition of the electronic system leads to highly non-Markovian dynamics. The non-Markovianity is related to the backflow of information from the baths to the system. In the case of this electronic partition, it results from the possible recurrence of a partial vibrational wave packet in the initial Franck-Condon region during the nonadiabatic dynamics. This leads to a signature in different measures of non-Markovianity [27,78,79]. It is related to the shape of the correlation function, which is the Fourier transform of the thermal spectral density and therefore depends on the occurrence of sharp peaks leading to a long oscillatory decay of $C(t)$ and thus a long memory timescale. This strong interaction between the system and the baths requires efficient non-Markovian approaches and is dealt with using the HEOM method. The key point is the expression of the correlation function of each bath b as a sum of $n_{\mathrm{cor},b}$ decay modes associated with the poles of the thermal spectral density (poles of the spectral density and of the Bose function also called Matsubara frequencies)

$$C_{t\,(c)}(t) = \sum_{k=1}^{n_{\mathrm{cor},t\,(c)}} \alpha_{t\,(c),k} e^{i\gamma_{t\,(c),k} t}. \qquad (10)$$

The HEOM method is well documented in the literature [38,40,41,53,56,80–85]. We adapt the HEOM algorithm by using a particular definition of the complex conjugate in which the rates remain the same in both expressions

$$C_{t\,(c)}^*(t) = \sum_{k=1}^{n_{\mathrm{cor},t\,(c)}} \tilde{\alpha}_{t\,(c),k} e^{i\gamma_{t\,(c),k} t}. \qquad (11)$$

Analytical expressions of the α_k, $\tilde{\alpha}_k$, and γ_k are given in Refs. [77,86]. We summarize the operational equations in Appendix A, paying particular attention to the backward propagation used in OCT. The corresponding expressions in the TT representation are given in Appendix B.

Methods similar to HEOM operate by tracing out the bath degrees of freedom. However, even if the vibrational dynamics is not completely resolved, important information

pertaining to the bath is available, for instance, heat current or fluxes [82,83,87,88]. The extraction and visualization of the time-dependent thermal probability distributions $P_m(X_b, t)$ of each collective mode $b = t, c$ in each electronic state m is an interesting tool to analyze non-Markovian dynamics [71,89]. Here $P_m(X_b, t)$ is expanded in the basis set of the eigenfunctions of the Ornstein-Uhlenbeck operator of the stochastic Liouville equation

$$P_m(X_b, t) = \sum_l a_{m,b,l}(t)\Phi_l(X_b), \qquad (12)$$

with $\Phi_l(X_b) = \frac{1}{\sqrt{2\pi}\sqrt{2^l l!}} H_l[X_b/\sqrt{2C_b(0)}]e^{-X_b^2/2C_b(0)}$, where the Hermite polynomials H_l are weighted by a temperature-dependent factor via the initial value of $C_b(t)$, which is the integral of the thermal spectral density. The computation may require HEOM at a high level when the distribution is far from the equilibrium Gaussian distribution. The expression of the $a_{m,b,l}(t)$ coefficients is given in Appendix A.

In particular, this first moment providing the average position of the coupling effective mode in each electronic state $\langle X_b^m \rangle$ is obtained from the auxiliary density operators (ADOs) of the first level for each bath

$$\mathbf{B}_b(t) = -\sum_{\mathbf{n}} \rho_{\mathbf{n}}(t), \qquad (13)$$

where the sum runs over all the collective index $\mathbf{n}$ for which $\sum_k n_{k,b} = 1$, with $b = t$ or $b = c$, respectively. The average in each electronic state is then given by the corresponding diagonal element

$$\langle X_b^{(m)} \rangle = \frac{1}{D_{0b}^{(m)}}(\mathbf{B}_b)_{mm}, \qquad (14)$$

where D_{0b} is given by $D_{0t(c)}^2 = (2/\pi)\int_0^\infty J_{t(c)}(\omega)\omega\, d\omega$. This average is an interesting bit of information about the vibrational relaxation and the evolution towards equilibrium. By expressing all the density matrices in Eq. (13) in the basis set of the localized diabatic states $D_{L(R)}$ via the transformation matrix U given in Eq. (7), one gets the average position in each left or right diabatic well showing the dissymmetry of the damped wave packet when the superposition $|\pm\rangle = (|S_1\rangle \pm |S_2\rangle)/\sqrt{2}$ is created. The electronic dissymmetry is estimated by the parameter

$$\Delta_X = \frac{1}{t_{\text{lim}}}\int_0^{t_{\text{lim}}} \left(\langle X_c^{(D_R)}\rangle + \langle X_c^{(D_L)}\rangle\right)dt, \qquad (15)$$

where t_{lim} has been fixed at 100 fs in this application.

The HEOM summarized in Appendix A are propagated at $T = 298$ K by the Cash-Karp-Runge-Kutta algorithm [45] by a homemade parallelized FORTRAN code. In Sec. V D we explore the implementation referring to the tensor-train approach. The HEOM adapted to this formulation are given in Appendix B. The propagation in the TT representation is made by the projector-splitting KSL scheme [47,48,90], designated by the three letters given to the three steps of the symmetrized splitting of second-order scheme also implemented in the TTPY package (tt.ksl.ksl) [91]. The number of matrices for K decay modes [Eq. (A2)] is then $N = \frac{(L+K)!}{L!K!}$. In the TT approach, n_{max} is the same for each mode, leading to

a larger number of matrices $N' = n_{\text{max}}^K$. The TT representation is expected to reduce the storage resources (see Appendix B).

IV. FIELD-DRIVEN DYNAMICS

Our objective is the depletion of the initial ground state and the creation of a coherent superposition of the excited states $|\pm\rangle = (|S_1\rangle \pm |S_2\rangle)/\sqrt{2}$. States $S_1(1B_2)$ and $S_2(2A_1)$ are excited by orthogonal transition dipole moments $\mu_y = 3.96ea_0$ and $\mu_z = -1.83ea_0$, respectively, the axes being defined in Fig. 1. The molecule is in the plane Oyz orthogonal to the propagation direction Ox of the electromagnetic waves, as indicated in Fig. 1. The time-dependent system Hamiltonian becomes $H_S(t) = H_S + V(t)$, where the interaction with the electromagnetic field $\vec{\mathcal{E}}(t)$ is written in length gauge and within the dipole approximation. In a V-type system at frozen equilibrium geometry, the superposition could be prepared by two pulses with orthogonal polarizations and integrated Rabi frequencies equal to $\pi/\sqrt{2}$ in the absence of interference with another bright state. This has been shown for pulses of duration τ and sine-square envelopes $\mathcal{E}_{y(z)}(t) = \mathcal{E}_{0,y(z)}\sin^2(\frac{\pi t}{\tau})\cos(\omega_{y(z)}t + \phi_{y(z)})$ [63]. The maximum amplitudes are then given by $\mathcal{E}_{0,y(z)} = \sqrt{2}\pi/\mu_{y(z)}\tau$. When the pulses have the same duration, the field amplitudes are then in the inverse ratio of the dipole transition moments. However, for ultrashort pulses with one or two optical cycles, one must ensure a zero-area laser pulse [92,93]. The field

$$\mathcal{E}_{y(z)}(t) = -\frac{\partial\mathcal{A}_{y(z)}(t)}{\partial t} \qquad (16)$$

is then derived from the vector potential $\mathcal{A}_{y(z)}(t) = (\frac{\mathcal{E}_{0,y(z)}}{\omega})\sin^2(\frac{\pi(t-t_i)}{\tau})\sin[\omega(t-t_i) + \phi]$, where t_i is the initial time of the pulse.

The best superposition would be obtained by ultrashort pulses to fight against the decoherence induced by the baths. However, the spectral band should not exceed 0.25 eV to avoid any contamination with neighboring states. We therefore focus on pulses of several tens of femtoseconds during which interaction with the vibrational motions occurs. The first strategy involves positive or negative chirp pulses with a linear variation of the carrier frequency. For commodity, we introduce a factor f that remains close to one and the time-dependent frequency is expressed by

$$\omega(t) = \frac{\omega_{y(z)}}{f} - \frac{\omega_{y(z)}/f - f\omega_{y(z)}}{\tau}t, \qquad (17)$$

where $\omega_{y(z)}$ is the carrier frequency in resonance with the two transitions. The chirp rate $\omega' = (\omega_{y(z)}/f - f\omega_{y(z)})/\tau$ is positive or negative according to $f > 1$ or $f < 1$.

In the second step, the best chirped pulses are taken as guess fields for optimization by OCT [42,94]. The optimal field is built iteratively to maximize the cost functional also called performance index or objective index

$$I = \text{Re}\{\text{Tr}[\rho^\dagger(\tau)\rho_{\text{target}}]\} \qquad (18)$$

at a final time τ with constraints to restrain the field intensity and to fulfill the master equation at any time. The corresponding Lagrange multipliers are denoted by α and $\chi(t)$, respectively. The optimal field is obtained from the system matrix density propagated by the master equation with initial
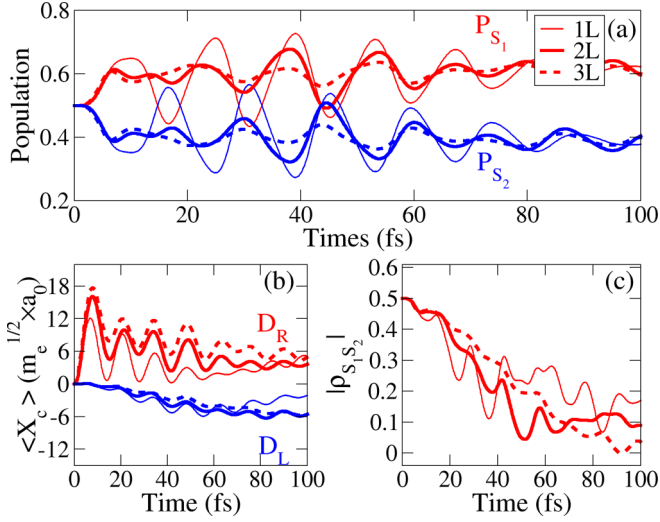
FIG. 3. Field-free so-called ideal case where the system is prepared in the superposed state $|+\rangle = (|S_1\rangle + |S_2\rangle)/\sqrt{2}$. A comparison of the dynamics with three spectral density models is made by retaining for each bath the highest frequency peak (1L, displayed by the thin solid line), the two highest frequency peaks (2L, displayed by the thick solid line), and the full density (3L, displayed by the dashed line) (see Fig. 2). (a) Population in the excited electronic states S_1 (red) and S_2 (blue). (b) Average position of the coupling mode in the localized diabatic states D_R (red) and D_L (blue). (c) Modulus of the electronic coherence between the two excited states (21) and (22).

condition $\rho(t = 0) = \rho_{\text{ini}}$ and from the Lagrange multiplier propagated with a final condition $\chi(\tau) = \rho_{\text{target}}$. The HEOM adapted for forward or backward propagations are given in Appendix A and the corresponding TT representation is in Appendix B. The field at each iteration k is obtained by $\varepsilon^{(k)} = \varepsilon^{(k-1)} + \Delta\varepsilon^{(k)}$, where $\Delta\varepsilon^{(k)}$ is estimated by

$$\Delta\varepsilon(t) = \frac{1}{\alpha}\text{Im}\left\{\text{Tr}[\rho(t)\chi(t)]\text{Tr}\left[\chi(t)\left(\sum_p \mu_p, \rho(t)\right)\right]\right\},$$
(19)

where $p = y, z$ [42].

V. RESULTS

A. Field-free case

Figure 3 compares the field-free dynamics with the full or the truncated spectral density (see Fig. 2) by retaining only the highest-frequency region for the two baths around $2360c\,\text{cm}^{-1}$ (denoted by 1L), the two highest peaks by adding those around $1700c\,\text{cm}^{-1}$ (2L), and the full density (3L). This is the so-called ideal case when the initial condition is the superposition

$$|+\rangle = (|S_1\rangle + |S_2\rangle)/\sqrt{2}$$
(20)

corresponding to a population on the right side D_R. We compare the populations of the excited states $P_{S_1}(t)$ and $P_{S_2}(t)$ [Fig. 3(a)], the average position of the coupling mode in the localized D_L and D_R states [Fig. 3(b)], and the modulus of the coherence $|\rho_{S_1S_2}(t)|$ [Fig. 3(c)]. The coherence

$$\rho_{S_1S_2}(t) = \rho_{S_2S_1}^*(t)$$
(21)

is the off-diagonal element corresponding to the two excited states denoted by S_1 and S_2 of the system reduced density matrix

$$\rho(t) = \text{Tr}_B[\rho_{\text{tot}}(t)],$$
(22)

which is the trace over the bath modes of the full density matrix. In the target state [Eq. (20)] the coherence is $|\rho_{S_1S_2}| = 0.5$. During the first 10 fs, the dynamics is dominated by the high-frequency mode. After this early relaxation, the population exchange is reduced when the lower frequency around $1700c\,\text{cm}^{-1}$ is considered. The modifications induced by the lowest-frequency region are less significant and we adopt a compromise by retaining two peaks for each bath (2L) in order to reduce the computational cost. Indeed, the partition adopted here leads to a very high system-bath coupling demanding a high level in the HEOM propagation [70,71]. The HEOM are carried out at level 12 without Matsubara terms in the correlation function. Retaining only two Lorentzians per bath (2L) involves 1.3×10^5 matrices versus 2.7×10^6 matrices in the 3L model. In the field-free case, the thermal equilibrium populations of the excited manifold are reached in 250 fs. The final populations are 0.39 for S_2 and 0.61 for S_1. We have verified that the equilibrium populations are the same for any initial excited state. These values do not correspond to a thermal Boltzmann mixture since the ground state is not coupled by nonadiabatic couplings with the excited states and the radiative decay is neglected. When we describe the excitation by laser pulses in the following sections, the population at equilibrium is different when the ground state is not completely depleted. The coherence decays in about 100 fs and the dissymmetry remains during the same period before leading finally to an equilibrium symmetric distribution in each well. The full distributions $P_{D_L}(X_c, t)$ and $P_{D_R}(X_c, t)$ [Eq. (12)] of the coupling mode in the D_L and D_R states are given in Figs. 4(a) and 4(b). This requires performing HEOM at least at level 15 to converge the expansion of Eq. (12). For this ideal case, the right side is populated and the oscillation persists for 40 fs before the transition towards the left side. For a simple statistical mixture with equal weights of the two states and no coherence, the populations are always identical in both localized states.

B. Chirped laser pulses

Figures 4(c) and 4(d) give the distributions $P_{D_L}(X_c, t)$ and $P_{D_R}(X_c, t)$ when the system is initially in the ground electronic state with the vibrational baths at thermal equilibrium at the equilibrium geometry and excited by two polarized pulses along y or z with $\tau = 10$ fs and amplitudes satisfying the $\pi/\sqrt{2}$ rule. When the system is excited by the pulses, one has a first delay of about 5 fs during the depopulation of the ground state before observing a notable density on the right side and the symmetry breaking has a lifetime shorter than in the field-free ideal case.

The first control against the decoherence during the interaction with the field is done by chirped pulses. For different pulse durations τ, the amplitudes of the two pulses are fixed by the $\pi/\sqrt{2}$ rule and we impose a positive- or negative-frequency chirp with a rate fixed by the f factor [Eq. (17)]. The efficiency is measured by the dissymmetry parameter
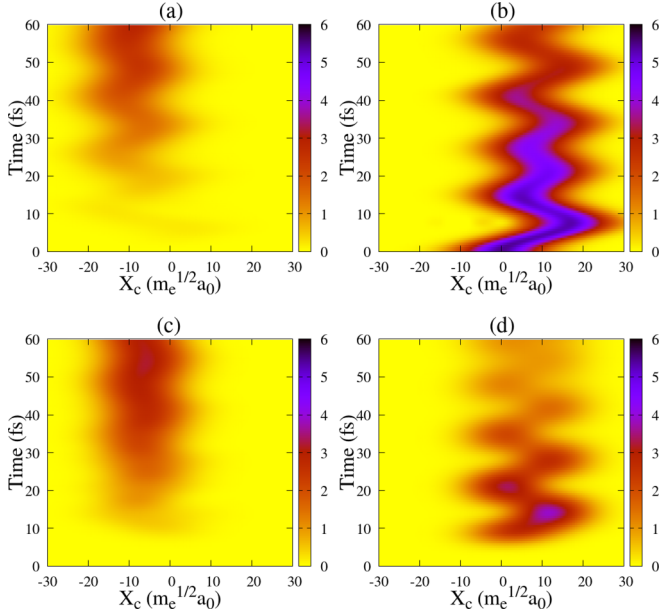
FIG. 4. Distributions $P_{D_L}(X_c, t)$ and $P_{D_R}(X_c, t)$ of the coupling collective mode in the localized excited states (model 2L). (a) and (b) Ideal case with the initial condition $|+\rangle = (|S_1\rangle + |S_2\rangle)/\sqrt{2}$ corresponding to the population in the right site D_R and (c) and (d) excitation from the ground state by two polarized pulses of 10 fs and amplitudes satisfying the $\pi/\sqrt{2}$ condition, in (a) and (c) the localized state D_L and (b) and (d) the localized state D_R. The color bar gives $P \times 10^2$.

Δ_X [Eq. (15)] presented in Fig. 5. For the ideal case $\Delta_X = 2.30 m_e^{1/2} a_0$. A negative value does not mean that the initial localization is not on the right side but that later transitions may induce a large oscillation on the left side. Whatever the sign, a nonzero value confirms the existence of a dissymmetry linked to a residual coherence. The positive chirp increases the dissymmetry only for τ in the range 10–35 fs. For longer
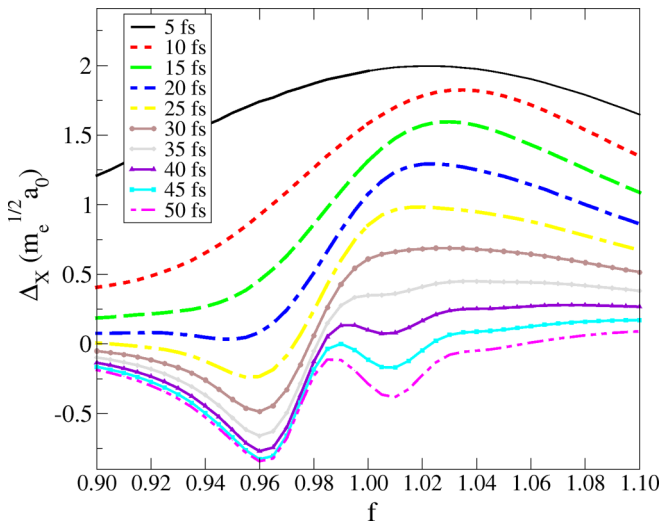

FIG. 5. Electronic dissymmetry Δ_X (in $m_e^{1/2} a_0$) defined by Eq. (15) for two polarized pulses along y or z with positive ($f > 1$) and negative ($f < 1$) chirps. The f factor determining the chirp rate is given in Eq. (17).
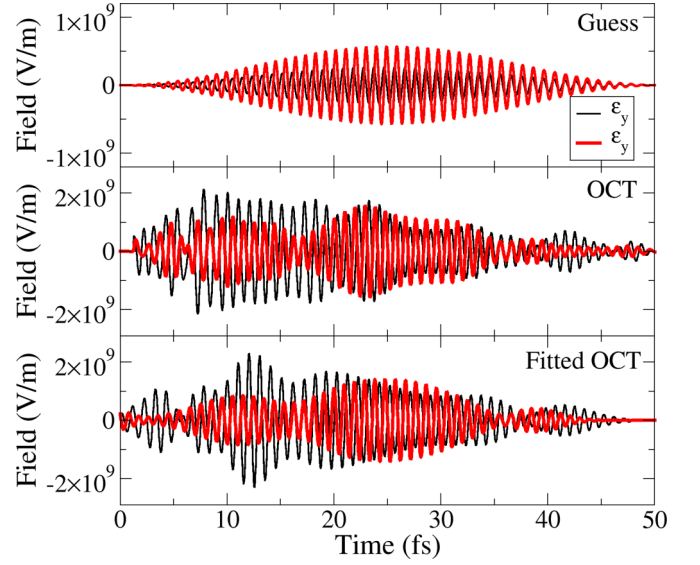

FIG. 6. Optimal fields $\mathcal{E}_y$ (thin black line) and $\mathcal{E}_z$ (thick red line) obtained when the guess fields are pulses of 50 fs with a negative chirp with $f = 0.962$ [Eq. (17)]. The fit is obtained with six Gaussian pulses for each polarization. The parameters are given in the Supplemental Material [66].

pulses (35–50 fs) that exceed the coherence lifetime of the ideal case, the efficiency is very weak in the absence of any chirp ($f = 1$). Negative chirps slightly improve the result.

In the following section, we select three pulses of 50, 15, and 10 fs with the chirp factor f giving the maximum absolute value of Δ_X. The first is longer than the decoherence time of the ideal case and the second one corresponds to the vibrational period of the effective coupling mode. These pulses are guess fields for an optimization by OCT to check which kind of restructuring is finally obtained.

C. Optimal control

The target reduced density matrix ρ_{target} at the end of the pulses τ is the one corresponding to the superposition $|+\rangle = (|S_1\rangle + |S_2\rangle)/\sqrt{2}$ with zero population in the initial equilibrium ground state. Our strategy is to let OCT optimize the y and z fields on a time grid. The objective index I [Eq. (18)] is never 100% (i.e., $|\rho_{S_1 S_2}| = 0.5$) because we limit the field amplitude to an upper value of 10^{-2} a.u. (5.1422×10^9 V m^{-1}) corresponding to an intensity of 3.51×10^{12} W cm^{-2}. The OCT fields obtained from the 50-, 15-, and 10-fs chirped guess fields and their fits are presented in Figs. 6, 7, and 8, respectively. We then fit the optimal fields for each polarization with a sequence of N_G simple Gaussian pulses with central time T_M,

$$\mathcal{E}_{y(z)}^{\text{fit}}(t) = \sum_i^{N_G} \varepsilon_{0_i} e^{-(t-t_{M_i})^2/2\sigma_i^2} \cos[\omega_i(t - t_{M_i})]. \quad (23)$$

The optimally fitted parameters ε_{0_i}, t_{M_i}, σ_i, and ω_i are given in the Supplemental Material [66]. We use the trust region reflective algorithm of the PYTHON module `scipy.optimize` to fit the optimal fields. The algorithm uses nonlinear least squares to fit data to a functional form [95,96]. In each case,
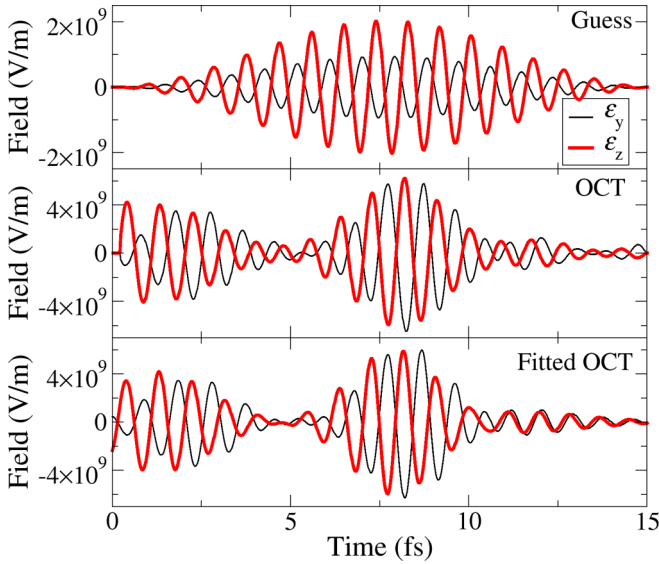
FIG. 7. Optimal fields $\mathcal{E}_y$ and $\mathcal{E}_z$ obtained when the guess fields are pulses of 15 fs with a positive chirp with $f = 1.03$ [Eq. (17)]. The fit is obtained with three Gaussian pulses for each polarization. The parameters are given in the Supplemental Material [66].

OCT strongly reshapes the simple chirped pulses and suggests a sequence of pulses with nearly the same delay for both polarisations. The rms of the fits is very good. It is given with all the parameters in the Supplemental Material [66]. The fitted fields with a pulse sequence are not fully identical but they retain the main features of the dynamics as seen in Figs. 9–11, where dynamics are compared.

(i) In the 50-fs case, the penalty factor is $\alpha = 5 \times 10^3$ [Eq. (19)]. The performance index [Eq. (18)] after 50 iterations is $I = 84\%$ providing a coherence of 0.34. Modifying
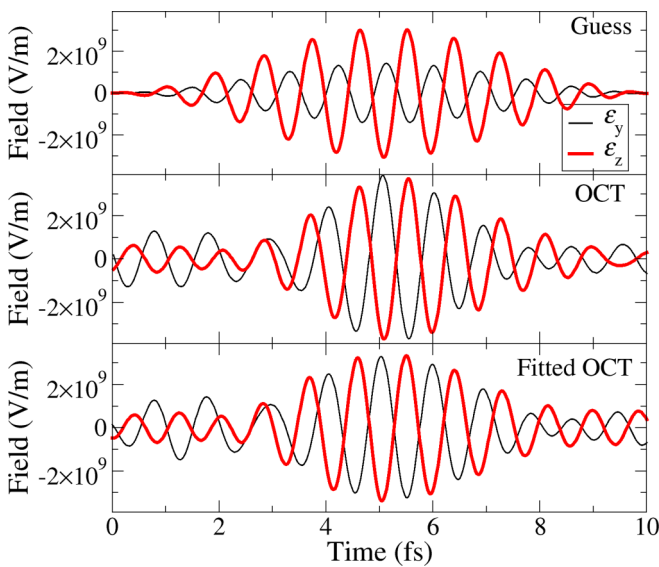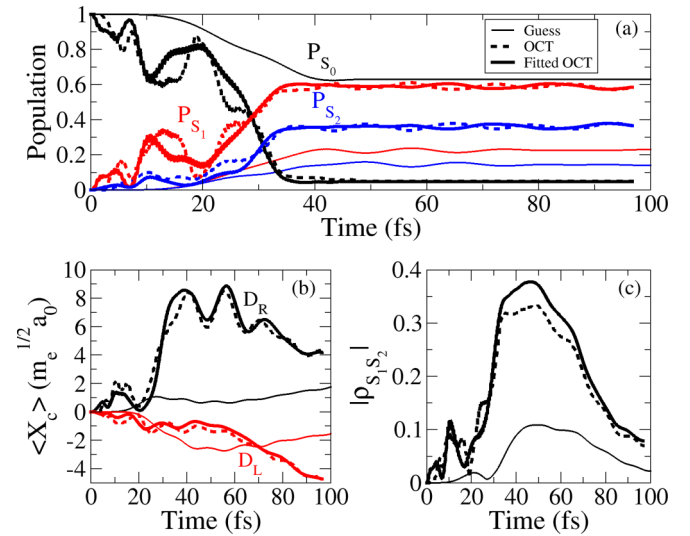

FIG. 9. Comparison between the dynamics driven by the chirped y and z pulses of 50 fs with $f = 0.962$ [Eq. (17)], the optimal pulses obtained with these guess fields, and the sequence of six Gaussians pulses fitting each OCT pulse. (a) Population in the ground state S_0 (black) and the excited electronic states S_1 (red) and S_2 (blue). (b) Average position of the coupling mode in the localized diabatic states D_R (black) and D_L (red). (c) Modulus of the electronic coherence between the two excited states (21) and (22).

α only influences the rate of convergence, but the optimal coherence never exceeds about 0.35 but nevertheless remains three time higher than the value given by the guess field. The creation of the coherence is more difficult for long pulses. However, the dissymmetry of the average value of the coupling mode on both sides is more striking for the long pulses. The OCT notably improves the depletion of the ground state,
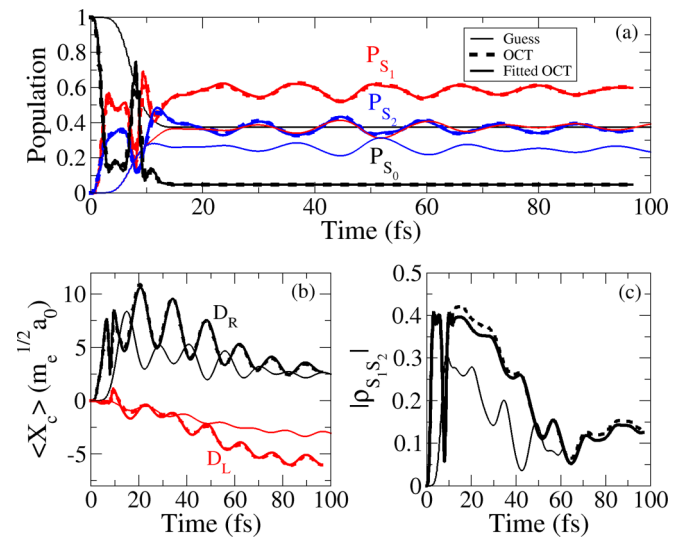

FIG. 8. Optimal fields $\mathcal{E}_y$ and $\mathcal{E}_z$ obtained when the guess fields are pulses of 10 fs with a positive chirp with $f = 1.04$ [Eq. (17)]. The fit is obtained with three Gaussian pulses for each polarization. The parameters are given in the Supplemental Material [66].

FIG. 10. Comparison between the dynamics driven by the chirped y and z pulses of 15 fs with $f = 1.03$ [Eq. (17)], the optimal pulses obtained with these guess fields, and the sequence of three Gaussians pulses fitting each OCT pulse. The description of each panel is the same as in Fig. 9.

FIG. 11. Comparison between the dynamics driven by the chirped y and z pulses of 10 fs with $f = 1.04$ [Eq. (17)], the optimal pulses obtained with these guess fields, and the sequence of three Gaussians pulses fitting each OCT pulse. The description of each panel is the same as in Fig. 9.
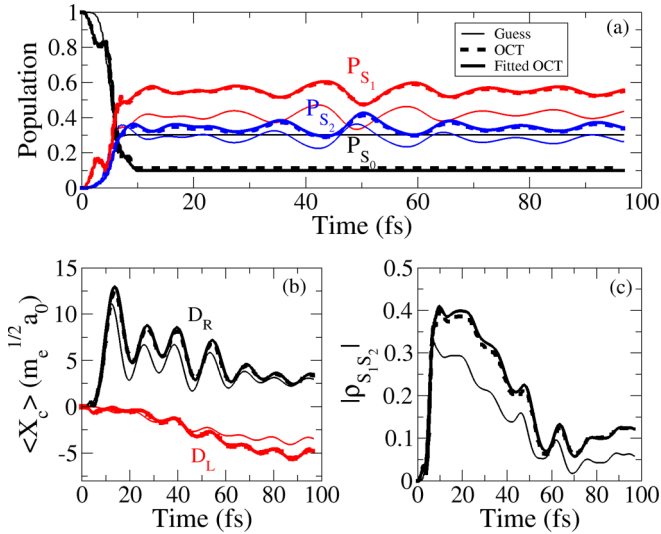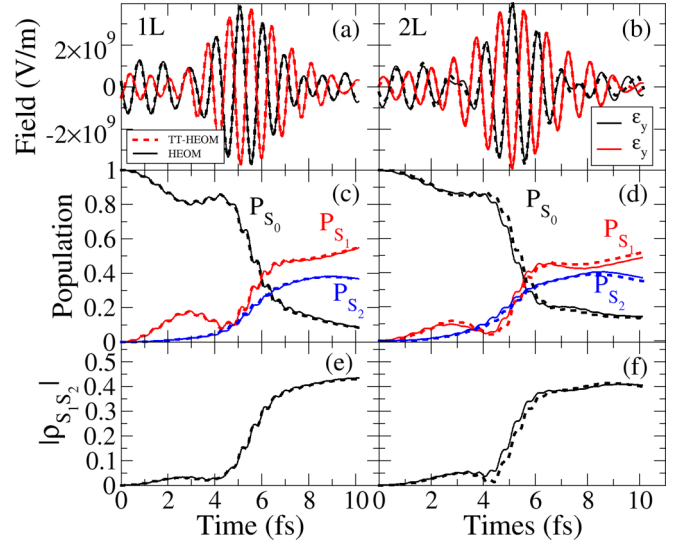

FIG. 12. Comparison between the dynamics performed by the adaptive Runge-Kutta method (HEOM) and TT simulation (TT-HEOM) with 10-fs pulse duration when the spectral densities are approximated by one (1L) or two (2L) Lorentzians. The HEOM level is 8. The OCT is driven in 50 iterations with $\alpha = 2 \times 10^4$ for 1L and 30 iterations with $\alpha = 1 \times 10^4$ for 2L.

the residual population being about 0.05 versus 0.62 with the chirped pulse. The OCT field consists of six pulses (around 5, 10, 17, and 29 fs) roughly corresponding to two pulses per vibrational period (14 fs).

(ii) In the 15-fs case, with $\alpha = 1 \times 10^4$ one gets $I = 89\%$ and a coherence of 0.42 after 150 iterations. The creation of the coherence is better for the short pulses, i.e., 0.42 as compared to 0.28. The residual population in the ground state is about 0.05 versus 0.38. The reshaping is particularly striking in this case leading to two main pulses for each polarization.

(iii) In the 10-fs case, with $\alpha = 2 \times 10^4$, $I = 87\%$ with a coherence of 0.43 versus 0.29 after 30 iterations. The improvement is less spectacular. Even for this short duration, OCT reshapes the field, suggesting a central shorter pulse of higher amplitude in a train of three pulses.

In all the previous examples, the simultaneous addressing of the two electronic states by the two polarizations is maintained in the OCT fields. To check the stability of this result, we also use a sequence of pulses with the two alternating polarizations and the same duration. Without a bath, the first $\pi/2$ pulse polarized along z makes a superposition of the ground and one excited state. Then a π pulse polarized along y in resonance with the second transition inverts the population of the ground and the second excited state. This guess field is less efficient than the simultaneous chirped pulses. The interesting result is that OCT reshapes the fields by mixing the polarization from the beginning. This is illustrated for a sequence of total duration of 15 fs in the Supplemental Material [66].

D. OCT by tensor trains

Finally, in the 10-fs case (see Fig. 11) we compare the simulations with the usual Cash-Karp-Runge-Kutta (denoted by HEOM) and the TT implementation (denoted by TT-

HEOM) described in Appendix B. For these fast dynamics, the behavior is very similar when the spectral densities are approximated by one or two Lorentzians, namely, the model 1L or 2L discussed above (see Fig. 3). In the 1L case, the optimization is made in 50 iterations with $\alpha = 2 \times 10^4$. In the 2L case, we consider 30 iterations with $\alpha = 1 \times 10^4$ (α is decreased to speed up the optimization rate). The HEOM level is 8 in each example. The dynamics are compared in Figs. 12(a), 12(c), and 12(e) for 1L and in Figs. 12(b), 12(d), and 12(f) for 2L. As one could notice, adaptive Runge-Kutta method HEOM, displayed by thin solid lines, and TT simulations, shown by dotted lines, give roughly the same fields, the same populations, and the same coherences. For both cases 1L and 2L, we obtain similar encouraging results. However, it is difficult to ensure good convergence when the spectral density presents several peaks. The ordering of the modes may be an important factor influencing the efficiency of time-dependent variational principle methods [97]. Further improvements are currently underway to consider the reorganization of the modes [73,98], rank adaptive methods [37,56,99–101], or hierarchical tensor-train approach [55].

VI. CONCLUSION

This work has addressed the laser control of the electronic symmetry breaking inducing a localization and a transitory oscillation on a given side of a symmetric dimer. The target initial electronic state is a superposed state of two nearly degenerate bright states coupled through a conical intersection. An initial superposition with equal weights of the delocalized excited adiabatic states in phase (plus sign) or out of phase (minus sign) corresponds to a localized diabatic state with electronic density on one side or the other of the symmetric dimer. Preparing a superposition means maintaining the electronic coherence during the control process. Ultrashort pulses

with a broad energy band are *a priori* more favorable, but they may interfere with additional bright states. We mainly considered control extending several tens of femtoseconds to ensure a width of about 0.25 eV. Then decoherence occurs during the pulses due to vibrational motions.

The control targets are the highest possible population in the excited manifold and the highest possible coherence (0.5 in our case) corresponding to the expected superposition, which induces the maximum dissymmetry. Based on experimental constraints concerning pulse shaping (frequency chirping rate and leading intensities) and the property of the V-type system with orthogonal transition dipole moments, we considered three steps. (i) We examined guess fields inspired by mechanisms whose efficiency is well known in the absence of baths: simultaneous pulses linearly polarized along orthogonal directions with negative or positive linear chirps and fulfilling for their amplitudes the $\pi/\sqrt{2}$ time integration condition, or a sequence of $\pi/2$ and π pulses with alternative polarization. (ii) We used these guess fields to initiate an optimal control scheme to see the suggested reshaping. (iii) We checked the robustness of such fields by fitting them with a sequence of simple Gaussian pulses.

It is worth noting that the dissymmetry towards the right or the left side may be easily reversed by changing the sign of the pulse with polarization z coupling to state S_2 through μ_z. This phase inversion generates the superposed state with the minus sign and changes the populated localized side. This is verified for the guess field and for the corresponding OCT field.

The tensor-train representation is a very promising approach for solving HEOM as it tackles the dimensionality curse with respect to the necessary memory space. Moreover, the TT approach is a background for future implementation of deep learning algorithms [98]. We have explicated the TT representation of the HEOM for OCT. However, it turns out that the present molecular system is particularly demanding since the electron-nuclei partition leads to strong system-bath coupling and a high hierarchy level with the ensuing large number of ADOs and a structured spectral density with at least two important peaks per bath. We face several numerical difficulties and instabilities when addressing structured spectral densities. An adaptive rank is necessary during the propagation. We have improved the results by a mixed strategy including steps with the Runge-Kutta algorithm in the variational time-dependent KSL procedure to increase the ranks. Further developments with other adaptive methods are ongoing [99,100].

As the molecular system is of moderate size, in principle, the full quantum dynamics with the LVC model could be performed by the variational multilayer multiconfiguration time-dependent Hartree method [102] with thermal average over initial conditions. Similar results are expected for very short laser pulses, mainly before the so-called Zeno time [103]. However, it is not clear whether the thermalization is treated on an equal footing in the wave packet with initial time average and in the open quantum system. Noise could also be introduced in a stochastic time-dependent Schrödinger equation with an improved treatment of the thermalization [104].

On general grounds, one observes that OCT suggests interesting strategies that could eventually be quite different from

an initial guess. For the very smooth simultaneous y and z chirps at resonance, OCT reshapes the fields in a sequence of a few pulses of 5 or 10 fs, slightly off-resonance and addressing again simultaneously the two excited states. When the guess is a sequence of π and $\pi/2$ pulses addressing successively the two states, OCT confirms our first strategy based on simultaneous use of the two polarizations by mixing from the very beginning the y and z polarizations. Optical control theory suggests the number of individual pulses and the simultaneous use of the polarizations. In this work we have fitted Gaussian pulses on the OCT fields. However, the OCT fields do not fully reach the target. The following prospective step would be to optimize the parameters (amplitude, frequency, central position, and width) imposing only the number of pulses suggested by OCT.

The data that support this study are available on request from the authors.

APPENDIX A: HEOM FOR FORWARD AND BACKWARD PROPAGATION

The non-Markovian master equation for the reduced density matrix of the system $\dot{\rho}(t) = -\frac{i}{\hbar}\text{Tr}_B[\hat{H}, \rho_{\text{tot}}(t)]$, where $\rho_{\text{tot}}(t)$ is the full density matrix, is solved by a time-local system of coupled equations among auxiliary matrices arranged in a hierarchical structure. Each auxiliary matrix has the dimension of $\rho(t)$ and is labeled by a collective index

$$\mathbf{n} = \{n_1, \ldots, n_K\} \tag{A1}$$

specifying the phonon occupation number of each decay mode in each bath b,

$$K = \sum_b^{N_B} n_{\text{cor},b}, \tag{A2}$$

where N_B is the number of baths (here $N_B = 2$) and $b = t, c$ [see Eq. (10)]. The system density matrix has the index $\mathbf{n} = \{0, \ldots, 0\}$. Matrices with an occupation number rising or descending by one unit are the only ones connected in the hierarchy.

The non-Markovian forward equation of OCT is an equation with initial condition, which may be written $\dot{\rho}(t) = L_S\rho(t) + \int_0^t K(t, t')\rho(t')dt'$. The corresponding coupled equations of the HEOM with correlation functions [Eqs. (10) and (11)] and with $\hbar = 1$ are

$$\dot{\rho}_{\mathbf{n}} = L_S\rho_{\mathbf{n}} + i\sum_b^{N_B}\sum_{k=1}^{n_{\text{cor},b}} n_{k,b}\gamma_{k,b}\rho_{\mathbf{n}} - i\sum_b^{N_B}\left[S_b, \sum_{k=1}^{n_{\text{cor},b}} \rho_{\mathbf{n}_{k,b}^+}\right]$$

$$- i\sum_b^{N_B}\sum_{k=1}^{n_{\text{cor},b}} n_{k,b}\left(\alpha_{k,b}S_b\rho_{\mathbf{n}_{k,b}^-} - \tilde{\alpha}_{k,b}\rho_{\mathbf{n}_{k,b}^-}S_b\right), \tag{A3}$$

where $L_S \cdot := -i[H_S(t), \cdot]$ and the parameters α_k, $\tilde{\alpha}_k$, and γ_k are defined in Eqs. (10) and (11). The analytical expressions as a function of the spectral density parameters are given in Refs. [77,86]. The S_b operators are defined in Sec. III. The rising $\mathbf{n}_k^+ = \{n_1, \ldots, n_k + 1, \ldots, n_{n_{\mathrm{cor}}}\}$ and descending $\mathbf{n}_k^- = \{n_1, \ldots, n_k - 1, \ldots, n_{n_{\mathrm{cor}}}\}$ matrices are those for which the occupation number differs by one unit in the hierarchy $n_k \to n_k \pm 1$. The initial condition is assumed to be factorized $\rho_{\mathrm{tot}}(t_0) = \rho(t_0)\rho_{\mathrm{eq}}$, where ρ_{eq} is the Boltzmann equilibrium distribution at the chosen temperature. The separable initial condition is justified because the vibrational bath is initially at equilibrium and the electronic system is in the ground state decoupled from the excited manifold. It may also be valid in the case of an ultrafast Franck-Condon excitation.

The Lagrange multiplier of OCT is propagated with a final condition $\chi(t_f) = \rho_{\mathrm{target}}$ at the time $t = t_f$ (end of the laser pulse). The non-Markovian equation with a final equation involves a different memory term $\dot{\chi}(t) = L_S\chi(t) - \int_t^{t_f} K^\dagger(t, t')\chi(t')dt'$ corresponding to the following coupled equations:

$$\dot{\chi}_{\mathbf{n}} = L_S\rho_{\mathbf{n}} - i\sum_b^{N_B}\sum_{k=1}^{n_{\mathrm{cor},b}} n_{k,b}\gamma_{k,b}\rho_{\mathbf{n}} - i\sum_b^{N_B}\left[S_b, \sum_{k=1}^{n_{\mathrm{cor},b}}\rho_{\mathbf{n}_k^+}\right]$$
$$+ i\sum_b^{N_B}\sum_{k=1}^{n_{\mathrm{cor},b}} n_k\left(\alpha_{k,b}\rho_{\mathbf{n}_k^-}S_b - \tilde{\alpha}_{k,b}S_b\rho_{\mathbf{n}_k^-}\right). \tag{A4}$$

In practice they are solved backward starting from $\chi(t_f) = \rho_{\mathrm{target}}$ and all the auxiliary matrices are set equal to zero. The factorized condition is less obvious than for the forward preparation, but the final condition does not correspond to a new equilibrium state of the baths.

For each electronic state m the coefficients $a_{m,b,l}(t)$ in the expansion of the time-dependent thermal probability distributions $P_m(X_{t/c}, t)$ of each collective mode [Eq. (12)] are the corresponding diagonal element of a matrix built from the auxiliary operators $\mathbf{A}_{b,l}(t) = \frac{(-1)^l}{\sqrt{l!C_b^l(0)}}\sum_{\mathbf{n}}\frac{l!}{\Pi n_{k,b}}\rho_{\mathbf{n}}(t)$, where the sum $\sum_k n_{k,b} = l$ [71,82,83] runs over the index $\mathbf{n}$ for which the partial level of bath b is equal to l.

APPENDIX B: TENSOR TRAINS

As already suggested by Shi and co-workers [53–55] and later by Borelli and Dolgov [56], we investigate solving the hierarchical equations of motion (A3) and (A4) by using the so-called tensor-train decomposition (also referred to as the matrix product state in the quantum physics community [37,46–50,52,97,105]). The usual truncation of the hierarchy retains all the ADOs up to a level L, so the sum of the occupation number is equal to L.

1. Tensor-train representation of the density matrices

The HEOM formalism relies on a set of auxiliary matrices which is basically a multidimensional array $\rho_{\mathbf{n}}$, where $\mathbf{n}$ and K are defined in Eqs. (A1) and (A2), respectively. Instead of considering a set of density matrices of dimension $n \times n$, with n the number of states in the system Hamiltonian H_S, we flatten each matrix as an n^2 vector without loss of generality. This vectorized density matrix will be denoted by $\bar{\rho}_{\mathbf{n}}$ and each
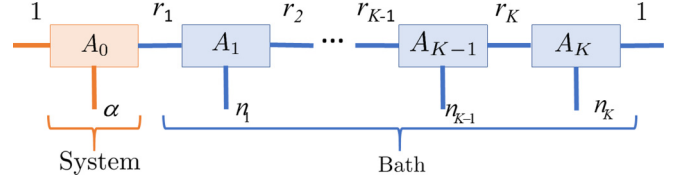

FIG. 13. Tensor-train decomposition schematization: A_k are the cores of the tensor; α runs from 1 to n^2, where n is the number of states in the system; and n_k is the index for each decay mode that runs from 0 to n_{max}.

of its element α ($\alpha \in [1, n^2]$) will be written in the TT format as

$$\bar{\rho}_{\mathbf{n}}^\alpha \approx \sum_{j_0}\sum_{j_1}\cdots\sum_{j_k}\cdots\sum_{j_{K+1}} A_0(j_0, \alpha, j_1)A_1(j_1, n_1, j_2) \times \cdots$$
$$\times A_k(j_k, n_k, j_{k+1})\cdots A_K(j_K, n_K, j_{K+1}). \tag{B1}$$

Here j_k goes from 1 to r_k, where r_k is the kth rank of the tensor (note that $r_0 = r_{K+1} = 1$ for dimensionality consistency). The A_k are called cores and consist in arrays of dimension $r_k \times n_e \times r_{k+1}$, where $n_e = n^2$ for $k = 0$ and $n_e = n_{\mathrm{HEOM}} = n_{\mathrm{max}} + 1$ for $k \neq 0$ (n_{HEOM} is the hierarchy order).

Tensor trains are often schematized as shown in Fig. 13 with the tensor network displaying a train shape where several cars are successively connected. Such decomposition is exact as long as the tensor ranks r_k grow without limitation. In practice, r_k are parameters during the simulation and one has to carefully check the convergence over them. Details on the mathematical background are beyond the scope of this article but they can be found in Refs. [47,48,51]. We heavily rely on the library TTPY developed in PYTHON and FORTRAN by Oseledets and co-workers [91]. It provides a user-friendly interface to build tensor trains, convert matrices (tt.matrix) and vectors (tt.vector) in TT format, and deal with the algebra of basic arithmetic operations ($+$, $-$, etc.) and Kronecker products (tt.kron) on TT-format objects.

To compute the system density matrix, we avoid a full expansion of $\bar{\rho}_{\mathbf{n}}^\alpha$ to overcome memory limitations. Instead, we make use of projectors in TT format

$$\mathcal{P}_\alpha = P_\alpha \otimes \prod_{j=1}^K V_j, \tag{B2}$$

where P_α is a vector of dimension n^2 with elements $P_{\alpha,l} = \delta_{\alpha,l}$ and V_j a vector of dimension n_{HEOM} with elements $V_{j,1} = 1$ if $l = 1$ and $= 0$ if $l \neq 1$. Thus, the elements of the system density vector are written

$$\bar{\rho}_{\mathbf{n}=\{0,\ldots,0,\ldots,0\}}^\alpha = \mathcal{P}_\alpha\bar{\rho}_{\mathbf{n}}. \tag{B3}$$

2. Time evolution

We solve the dynamic problem by using the projector-splitting KSL scheme [47,48,90] implemented in the TTPY package (tt.ksl.ksl) [91]. To use this algorithm, one has to provide a single superoperator which acts on the full TT-converted vector $\bar{\rho}_{\mathbf{n}}$ (or $\bar{\chi}_{\mathbf{n}}$ in the case of backward

propagation) representing all the auxiliary density operators such that

$$\frac{d}{dt}\bar{\rho}_{\mathbf{n}} = \mathcal{L}\bar{\rho}_{\mathbf{n}}, \tag{B4}$$

$$\frac{d}{dt}\bar{\chi}_{\mathbf{n}} = \mathcal{L}_b\bar{\chi}_{\mathbf{n}}. \tag{B5}$$

The Liouvillian superoperators $\mathcal{L}$ and $\mathcal{L}_b$ can be derived from the hierarchical set of equations of motions for both the forward [Eq. (B4)] and backward [Eq. (B5)] propagations. We provide below a summary of the essential equations to build these Liouvillian operators. It is worth mentioning that all the necessary arithmetic operations can be performed in the TT format.

a. Forward propagation

For the forward propagation, the associated Liouvillian (B6) denoted in our case as a superoperator $\mathcal{L}$ is written

$$\mathcal{L} = \mathcal{L}_S + \sum_{k'=1}^{K}(\mathcal{L}_{k'} + \mathcal{L}_{k'-} + \mathcal{L}_{k'+}), \tag{B6}$$

where $k' = (k, b)$ is a collective index which addresses both the index of the correlation function terms ($k \in [1, n_{\text{cor},b}]$) (see Eq.(10)) and the index of the bath ($b \in [1, N_B]$). Each of the terms in Eq. (B6) can be further derived as Kronecker products of various operators. In the following expressions, I_n denotes the identity matrix with dimensions $n \times n$, $\otimes$ is a matrix Kronecker product for two matrices, $\otimes \prod$ is an ordered (from left to right) sequence of Kronecker products, and $\delta_{l,m}$ is a Kronecker delta symbol ($\delta_{l,m} = 1$ if $l = m$ and 0 if $l \neq m$). The system Liouvillian is written

$$\mathcal{L}_S = -i(H_S \otimes I_n - I_n \otimes H_S) \otimes \prod_{k''=1}^{K} I_{n_{\text{HEOM}}}. \tag{B7}$$

The damping term is

$$\mathcal{L}_{k'} = i\gamma_{k',t\,(c)}I_{n^2} \otimes \prod_{k''=1}^{K} M_{k''}, \tag{B8}$$

where $M_{k''} = I_{n_{\text{HEOM}}}$ if $k'' \neq k'$ and $M_{k'',lm} = (l-1)\delta_{l,m}$ if $k'' = k'$ ($l, m \in [1, n_{\text{HEOM}}]$). The superoperator connecting the ADOs with an upper layer in the hierarchy is

$$\mathcal{L}_{k'+} = -i(S_{k'} \otimes I_n - I_n \otimes S_{k'}) \otimes \prod_{k''=1}^{K} M'_{k''}, \tag{B9}$$

where $M'_{k''} = I_{n_{\text{HEOM}}}$ if $k'' \neq k'$ and $M'_{k'',lm} = \delta_{l+1,m}$ if $k'' = k'$ ($l, m \in [1, n_{\text{HEOM}}]$). The superoperator connecting ADOs with a lower layer in the hierarchy is

$$\mathcal{L}_{k'-} = -i(\alpha_{k',t\,(c)}S_{k'} \otimes I_n - \tilde{\alpha}_{k',t\,(c)}I_n \otimes S_{k'}) \otimes \prod_{k''=1}^{K} M''_{k''}, \tag{B10}$$

where $M''_{k''} = I_{n_{\text{HEOM}}}$ if $k'' \neq k'$ and $M''_{k'',lm} = (l-1)\delta_{l-1,m}$ if $k'' = k'$ ($l, m \in [1, n_{\text{HEOM}}]$).

Finally, for pedagogical purpose, we provide in the Supplemental Material [66] a step-by-step derivation of the superoperators with a simplified two-dimensional system and a single tuning bath treated by HEOM at level 2.

b. Backward propagation

The very same procedure can be applied for the backward propagation. Thus, the backward Liouvillian $\mathcal{L}_b$ is written

$$\mathcal{L}_b = \mathcal{L}_S + \sum_{k'=1}^{K}(-\mathcal{L}_{k'} + \mathcal{L}_{bk'-} + \mathcal{L}_{k'+}), \tag{B11}$$

where the superoperator acting on a lower layer is slightly modified as

$$\mathcal{L}_{bk'-} = i(\alpha_{k',t\,(c)}I_n \otimes S_{k'} - \tilde{\alpha}_{k',t\,(c)}S_{k'} \otimes I_n) \otimes \prod_{k''=1}^{K} M''_{k''}. \tag{B12}$$

One can check by expanding $\mathcal{L}$ [Eq. (B6)] and $\mathcal{L}_b$ [Eq. (B11)] that Eqs. (B4) and (B5) are equivalent to Eqs. (A3) and (A4), respectively.

[1] S. Chelkowski, G. L. Yudin, and A. D. Bandrauk, Observing electron motion in molecules, J. Phys. B **39**, S409 (2006).

[2] F. Remacle and R. D. Levine, An electronic time scale in chemistry, Proc. Natl. Acad. Sci. USA **103**, 6793 (2006).

[3] F. Remacle, R. Kienberger, F. Krausz, and R. Levine, On the feasibility of an ultrafast purely electronic reorganization in lithium hydride, Chem. Phys. **338**, 342 (2007).

[4] I. S. Ulusoy and M. Nest, Correlated electron dynamics: How aromaticity can be controlled, J. Am. Chem. Soc. **133**, 20230 (2011).

[5] F. Bouakline and J. C. Tremblay, Is it really possible to control aromaticity of benzene with light? Phys. Chem. Chem. Phys. **22**, 15401 (2020).

[6] A. Palacios and F. Martín, The quantum chemistry of attosecond molecular science, WIREs Comput. Mol. Sci. **10**, e1430 (2020).

[7] I. C. D. Merritt, D. Jacquemin, and M. Vacher, Attochemistry: Is controlling electrons the future of photochemistry, J. Phys. Chem. Lett. **12**, 8404 (2021).

[8] C. Liu, J. Manz, K. Ohmori, C. Sommer, N. Takei, J. C. Tremblay, and Y. Zhang, Attosecond Control of Restoration of Electronic Structure Symmetry, Phys. Rev. Lett. **121**, 173201 (2018).

[9] D. Haase, G. Hermann, J. Manz, V. Pohl, and J. C. Tremblay, Electron symmetry breaking during attosecond charge migration induced by laser pulses: Point group analyses for quantum dynamics, Symmetry **13**, 205 (2021).

[10] M. A. Robb, A. J. Jenkins, and M. Vacher, *Attosecond Molecular Dynamics*, edited by M. J. J. Vrakking and F. Lepine (Royal Society of Chemistry, London, 2018), Chap. 8, pp. 275–307.

[11] C. Arnold, O. Vendrell, R. Welsch, and R. Santra, Control of Nuclear Dynamics through Conical Intersections and Electronic Coherences, Phys. Rev. Lett. **120**, 123001 (2018).

[12] S. Tomasi, S. Baghbanzadeh, S. Rahimi-Keshari, and I. Kassal, Coherent and controllable enhancement of light-harvesting efficiency, Phys. Rev. A **100**, 043411 (2019).

[13] W. Hu, B. Gu, and I. Franco, Toward the laser control of electronic decoherence, J. Chem. Phys. **152**, 184305 (2020).

[14] F. Schüppel, T. Schnappinger, L. Bäuml, and R. de Vivie-Riedle, Waveform control of molecular dynamics close to a conical intersection, J. Chem. Phys. **153**, 224307 (2020).

[15] A. Csehi, P. Badankó, G. J. Halasz, Á. Vibók, and B. Lasorne, On the preservation of coherence in the electronic wavepacket of a neutral and rigid polyatomic molecule, J. Phys. B **53**, 184005 (2020).

[16] G. E. Fux, E. P. Butler, P. R. Eastham, B. W. Lovett, and J. Keeling, Efficient Exploration of Hamiltonian Parameter Space for Optimal Control of Non-Markovian Open Quantum Systems, Phys. Rev. Lett. **126**, 200401 (2021).

[17] S. Machnes, U. Sander, S. J. Glaser, P. de Fouquières, A. Gruslys, S. Schirmer, and T. Schulte-Herbrüggen, Comparing, optimizing, and benchmarking quantum-control algorithms in a unifying programming framework, Phys. Rev. A **84**, 022305 (2011).

[18] R.-B. Wu, B. Chu, D. H. Owens, and H. Rabitz, Data-driven gradient algorithm for high-precision quantum control, Phys. Rev. A **97**, 042122 (2018).

[19] M. Bukov, A. G. R. Day, D. Sels, P. Weinberg, A. Polkovnikov, and P. Mehta, Reinforcement Learning in Different Phases of Quantum Control, Phys. Rev. X **8**, 031086 (2018).

[20] E. F. Thomas and N. E. Henriksen, Applying artificial neural networks to coherent control experiments: A theoretical proof of concept, Phys. Rev. A **99**, 023422 (2019).

[21] I. Paparelle, L. Moro, and E. Prati, Digitally stimulated Raman passage by deep reinforcement learning, Phys. Lett. A **384**, 126266 (2020).

[22] J. Chathanathil, G. Liu, and S. A. Malinovskaya, Semiclassical control theory of coherent anti-Stokes Raman scattering maximizing vibrational coherence for remote detection, Phys. Rev. A **104**, 043701 (2021).

[23] Q. Ansel, D. Sugny, and B. Bellomo, Exploring the limits of the generation of nonclassical states of spins coupled to a cavity by optimal control, Phys. Rev. A **105**, 042618 (2022).

[24] C. P. Koch, U. Boscain, T. Calarco, G. Dirr, S. Filipp, S. J. Glaser, R. Kosloff, S. Montangero, T. Schulte-Herbrüggen, D. Sugny, and F. K. Wilhelm, Quantum optimal control in quantum technologies. strategic report on current status, visions and goals for research in Europe, EPJ Quantum Technol. **9**, 19 (2022).

[25] C. P. Koch, Controlling open quantum systems: Tools, achievements, and limitations, J. Phys.: Condens. Matter **28**, 213001 (2016).

[26] B. Hwang and H.-S. Goan, Optimal control for non-Markovian open quantum systems, Phys. Rev. A **85**, 032321 (2012).

[27] E. Mangaud, R. Puthumpally-Joseph, D. Sugny, C. Meier, O. Atabek, and M. Desouter-Lecomte, Non-Markovianity in the optimal control of an open quantum system described by hierarchical equations of motion, New J. Phys. **20**, 043050 (2018).

[28] I. de Vega and D. Alonso, Dynamics of non-Markovian open quantum systems, Rev. Mod. Phys. **89**, 015001 (2017).

[29] K. H. Hughes, C. D. Christ, and I. Burghardt, Effective-mode representation of non-Markovian dynamics: A hierarchical approximation of the spectral density. II. Application to environment-induced nonadiabatic dynamics, J. Chem. Phys. **131**, 124108 (2009).

[30] I. Burghardt, R. Martinazzo, and K. H. Hughes, Non-Markovian reduced dynamics based upon a hierarchical effective-mode representation, J. Chem. Phys. **137**, 144107 (2012).

[31] F. Di Maiolo, D. Brey, R. Binder, and I. Burghardt, Quantum dynamical simulations of intra-chain exciton diffusion in an oligo (*para*-phenylene vinylene) chain at finite temperature, J. Chem. Phys. **153**, 184107 (2020).

[32] M. P. Woods, R. Groux, A. W. Chin, S. F. Huelga, and M. B. Plenio, Mappings of open quantum systems onto chain representations and Markovian embeddings, J. Math. Phys. **55**, 032101 (2014).

[33] D. Tamascelli, A. Smirne, J. Lim, S. F. Huelga, and M. B. Plenio, Efficient Simulation of Finite-Temperature Open Quantum Systems, Phys. Rev. Lett. **123**, 090402 (2019).

[34] F. Mascherpa, A. Smirne, A. D. Somoza, P. Fernández-Acebal, S. Donadi, D. Tamascelli, S. F. Huelga, and M. B. Plenio, Optimized auxiliary oscillators for the simulation of general open quantum systems, Phys. Rev. A **101**, 052108 (2020).

[35] P. Strasberg, G. Schaller, N. Lambert, and T. Brandes, Nonequilibrium thermodynamics in the strong coupling and non-Markovian regime based on a reaction coordinate mapping, New J. Phys. **18**, 073007 (2016).

[36] R. Borrelli and M. F. Gelin, Simulation of quantum dynamics of excitonic systems at finite temperature: An efficient method based on thermo field dynamics, Sci. Rep. **7**, 9127 (2017).

[37] T. Lacroix, A. Dunnett, D. Gribben, B. W. Lovett, and A. Chin, Unveiling non-Markovian spacetime signaling in open quantum systems with long-range tensor network dynamics, Phys. Rev. A **104**, 052204 (2021).

[38] Y. Tanimura and R. Kubo, Time evolution of a quantum system in contact with a nearly Gaussian-Markoffian noise bath, J. Phys. Soc. Jpn. **58**, 101 (1989).

[39] Y. Tanimura, Stochastic Liouville, Langevin, Fokker-Planck, and master equation approaches to quantum dissipative systems, J. Phys. Soc. Jpn. **75**, 082001 (2006).

[40] Y. Tanimura, Numerically "exact" approach to open quantum dynamics: The hierarchical equations of motion (HEOM), J. Chem. Phys. **153**, 020901 (2020).

[41] Q. Shi, L. Chen, G. Nan, R.-X. Xu, and Y. Yan, Efficient hierarchical Liouville space propagator to quantum dissipative dynamics, J. Chem. Phys. **130**, 084105 (2009).

[42] Y. Ohtsuki, W. Zhu, and H. Rabitz, Monotonically convergent algorithm for quantum optimal control with dissipation, J. Chem. Phys. **110**, 9825 (1999).

[43] Y. Ohtsuki, Non-Markovian effects on quantum optimal control of dissipative wave packet dynamics, J. Chem. Phys. **119**, 661 (2003).

[44] A. Chenel, E. Mangaud, I. Burghardt, C. Meier, and M. Desouter-Lecomte, Exciton dissociation at donor-acceptor heterojunctions: Dynamics using the collective effective mode representation of the spin-boson model, J. Chem. Phys. **140**, 044104 (2014).

[45] W. H. Press, S. A. Teukolsky, W. T. Vetterling, and B. P. Flannery, *Numerical Recipes: The Art of Scientific Computing* (Cambridge University Press, Cambridge, 1992).

[46] Y.-Y. Shi, L.-M. Duan, and G. Vidal, Classical simulation of quantum many-body systems with a tree tensor network, Phys. Rev. A **74**, 022320 (2006).

[47] C. Lubich, I. V. Oseledets, and B. Vandereycken, Time integration of tensor trains, SIAM J. Numer. Anal. **53**, 917 (2015).

[48] J. Haegeman, C. Lubich, I. Oseledets, B. Vandereycken, and F. Verstraete, Unifying time evolution and optimization with matrix product states, Phys. Rev. B **94**, 165116 (2016).

[49] F. A. Y. N. Schröder and A. W. Chin, Simulating open quantum dynamics with time-dependent variational matrix product states: Towards microscopic correlation of environment dynamics and reduced system evolution, Phys. Rev. B **93**, 075105 (2016).

[50] A. M. Alvertis, F. A. Y. N. Schröder, and A. W. Chin, Non-equilibrium relaxation of hot states in organic semiconductors: Impact of mode-selective excitation on charge transfer, J. Chem. Phys. **151**, 084104 (2019).

[51] S. Paeckel, T. Köhler, A. Swoboda, S. R. Manmana, U. Schollwöck, and C. Hubig, Time-evolution methods for matrix-product states, Ann. Phys. (NY) **411**, 167998 (2019).

[52] D. Quiñones-Valles, S. Dolgov, and D. Savostyanov, *Integral Methods in Science and Engineering: Analytic Treatment and Numerical Approximations*, edited by C. Constanda and P. Harris (Springer International, Cham, 2019), pp. 367–379.

[53] Q. Shi, Y. Xu, Y. Yan, and M. Xu, Efficient propagation of the hierarchical equations of motion using the matrix product state method, J. Chem. Phys. **148**, 174102 (2018).

[54] Y. Yan, T. Xing, and Q. Shi, A new method to improve the numerical stability of the hierarchical equations of motion for discrete harmonic oscillator modes, J. Chem. Phys. **153**, 204109 (2020).

[55] Y. Yan, M. Xu, T. Li, and Q. Shi, Efficient propagation of the hierarchical equations of motion using the Tucker and hierarchical Tucker tensors, J. Chem. Phys. **154**, 194104 (2021).

[56] R. Borrelli and S. Dolgov, Expanding the range of hierarchical equations of motion by tensor-train implementation, J. Phys. Chem. B **125**, 5397 (2021).

[57] J. C. Kirkwood, C. Scheurer, V. Chernyak, and S. Mukamel, Simulations of energy funneling and time- and frequency-gated fluorescence in dendrimers, J. Chem. Phys. **114**, 2419 (2001).

[58] T. Nelson, S. Fernandez-Alberti, A. E. Roitberg, and S. Tretiak, Electronic delocalization, vibrational dynamics, and energy transfer in organic chromophores, J. Phys. Chem. Lett. **8**, 3020 (2017).

[59] M. C. Aguilera, A. E. Roitberg, V. D. Kleiman, S. Fernandez-Alberti, and J. F. Galindo, Unraveling direct and indirect energy transfer pathways in a light-harvesting dendrimer, J. Phys. Chem. C **124**, 22383 (2020).

[60] G. Herzberg and H. C. Longuet-Higgins, Intersection of potential energy surfaces in polyatomic molecules, Discuss. Faraday Soc. **35**, 77 (1963).

[61] E. K.-L. Ho and B. Lasorne, Diabatic pseudofragmentation and nonadiabatic excitation-energy transfer in meta-substituted dendrimer building blocks, Comput. Theor. Chem. **1156**, 25 (2019).

[62] W. Domcke, D. Yarkony, and H. Koppel, *Conical Intersection: Theory, Computation and Experiment* (World Scientific, Hackensack, 2011).

[63] G. Breuil, E. Mangaud, B. Lasorne, O. Atabek, and M. Desouter-Lecomte, Funneling dynamics in a phenylacetylene trimer: Coherent excitation of donor excitonic states and their superposition, J. Chem. Phys. **155**, 034303 (2021).

[64] M. J. Frisch, G. W. Trucks, H. B. Schlegel, G. E. Scuseria, M. A. Robb, J. R. Cheeseman, G. Scalmani, V. Barone, G. A. Petersson, H. Nakatsuji, X. Li, M. Caricato, A. V. Marenich, J. Bloino, B. G. Janesko, R. Gomperts, B. Mennucci, H. P. Hratchian, J. V. Ortiz, A. F. Izmaylov *et al.*, *Gaussian˜16 Revision A.03* (Gaussian Inc., Wallingford, 2016).

[65] E. K.-L. Ho, T. Etienne, and B. Lasorne, Vibronic properties of *para*-polyphenylene ethynylenes: TD-DFT insights, J. Chem. Phys. **146**, 164303 (2017).

[66] See Supplemental Material at http://link.aps.org/supplemental/10.1103/PhysRevA.106.043121 for the Cartesian coordinates at the ground state equilibrium geometry and of the MECI at the CAM-B3LYP/6-31+G* level of theory, the gradients of the LVC model, the parameters of the spectral density fit and of the Gaussian pulses fitting the OCT fields, the expressions of the Liouvillian super-operators used in the tensor-train approach in a simple example.

[67] L. K. McKemmish, R. H. McKenzie, N. S. Hush, and J. R. Reimers, Quantum entanglement between electronic and vibrational degrees of freedom in molecules, J. Chem. Phys. **135**, 244110 (2011).

[68] B. Gonon, A. Perveaux, F. Gatti, D. Lauvergnat, and B. Lasorne, On the applicability of a wavefunction-free, energy-based procedure for generating first-order non-adiabatic couplings around conical intersections, J. Chem. Phys. **147**, 114114 (2017).

[69] L. Chen, M. F. Gelin, V. Y. Chernyak, W. Domcke, and Y. Zhao, Dissipative dynamics at conical intersections: Simulations with the hierarchy equations of motion method, Faraday Discuss. **194**, 61 (2016).

[70] H.-G. Duan and M. Thorwart, Quantum mechanical wave packet dynamics at a conical intersection with strong vibrational dissipation, J. Phys. Chem. Lett. **7**, 382 (2016).

[71] E. Mangaud, B. Lasorne, O. Atabek, and M. Desouter-Lecomte, Statistical distributions of the tuning and coupling collective modes at a conical intersection using the hierarchical equations of motion, J. Chem. Phys. **151**, 244102 (2019).

[72] J. Strümpfer and K. Schulten, The effect of correlated bath fluctuations on exciton transfer, J. Chem. Phys. **134**, 095102 (2011).

[73] A. J. Dunnett, D. Gowland, C. M. Isborn, A. W. Chin, and T. J. Zuehlsdorff, Influence of non-adiabatic effects on linear absorption spectra in the condensed phase: Methylene blue, J. Chem. Phys. **155**, 144112 (2021).

[74] R. Martinazzo, K. H. Hughes, F. Martelli, and I. Burghardt, Effective spectral densities for system-environment dynamics at conical intersections: S_2-S_1 conical intersection in pyrazine, Chem. Phys. **377**, 21 (2010).

[75] H. Tamura, R. Martinazzo, M. Ruckenbauer, and I. Burghardt, Quantum dynamics of ultrafast charge transfer at an oligothiophene-fullerene heterojunction, J. Chem. Phys. **137**, 22A540 (2012).

[76] W. Popp, M. Polkehn, K. H. Hughes, R. Martinazzo, and I. Burghardt, Vibronic coupling models for donor-acceptor aggregates using an effective-mode scheme: Application to mixed Frenkel and charge-transfer excitons in oligothiophene aggregates, J. Chem. Phys. **150**, 244114 (2019).

[77] C. Meier and D. J. Tannor, Non-Markovian evolution of the density operator in the presence of strong laser fields, J. Chem. Phys. **111**, 3365 (1999).

[78] E. Mangaud, C. Meier, and M. Desouter-Lecomte, Analysis of the non-Markovianity for electron transfer reactions in an oligothiophene-fullerene heterojunction, Chem. Phys. **494**, 90 (2017).

[79] R. Puthumpally-Joseph, E. Mangaud, V. Chevet, M. Desouter-Lecomte, D. Sugny, and O. Atabek, Basic mechanisms in the laser control of non-Markovian dynamics, Phys. Rev. A **97**, 033411 (2018).

[80] A. Ishizaki and Y. Tanimura, Quantum dynamics of system strongly coupled to low-temperature colored noise bath: Reduced hierarchy equations approach, J. Phys. Soc. Jpn. **74**, 3131 (2005).

[81] R.-X. Xu and Y. Yan, Dynamics of quantum dissipation systems interacting with bosonic canonical bath: Hierarchical equations of motion approach, Phys. Rev. E **75**, 031107 (2007).

[82] L. Zhu, H. Liu, W. Xie, and Q. Shi, Explicit system-bath correlation calculated using the hierarchical equations of motion method, J. Chem. Phys. **137**, 194106 (2012).

[83] H. Liu, L. Zhu, S. Bai, and Q. Shi, Reduced quantum dynamics with arbitrary bath spectral densities: Hierarchical equations of motion based on several different bath decomposition schemes, J. Chem. Phys. **140**, 134106 (2014).

[84] A. Ishizaki and G. R. Fleming, Unified treatment of quantum coherent and incoherent hopping dynamics in electronic energy transfer: Reduced hierarchy equation approach, J. Chem. Phys. **130**, 234111 (2009).

[85] T. Ikeda and G. D. Scholes, Generalization of the hierarchical equations of motion theory for efficient calculations with arbitrary correlation functions, J. Chem. Phys. **152**, 204101 (2020).

[86] A. Pomyalov, C. Meier, and D. J. Tannor, The importance of initial correlations in rate dynamics: A consistent non-Markovian master equation approach, Chem. Phys. **370**, 98 (2010).

[87] Q. Shi, L. Chen, G. Nan, R. Xu, and Y. Yan, Electron transfer dynamics: Zusman equation versus exact theory, J. Chem. Phys. **130**, 164518 (2009).

[88] L. Song and Q. Shi, Hierarchical equations of motion method applied to nonequilibrium heat transport in model molecular junctions: Transient heat current and high-order moments of the current operator, Phys. Rev. B **95**, 064308 (2017).

[89] A. Chin, E. Mangaud, V. Chevet, O. Atabek, and M. Desouter-Lecomte, Visualising the role of non-perturbative environment dynamics in the dissipative generation of coherent electronic motion, Chem. Phys. **525**, 110392 (2019).

[90] C. Lubich and I. V. Oseledets, A projector-splitting integrator for dynamical low-rank approximation, BIT Numer. Math. **54**, 171 (2014).

[91] https://github.com/oseledets/ttpy.

[92] T. Brabec and F. Krausz, Intense few-cycle laser fields: Frontiers of nonlinear optics, Rev. Mod. Phys. **72**, 545 (2000).

[93] D. B. Milošević, G. G. Paulus, D. Bauer, and W. Becker, Above-threshold ionization by few-cycle pulses, J. Phys. B **39**, R203 (2006).

[94] W. Zhu, J. Botina, and H. Rabitz, Rapidly convergent iteration methods for quantum optimal control of population, J. Chem. Phys. **108**, 1953 (1998).

[95] https://docs.scipy.org/doc/scipy/reference/generated/scipy.optimize.curve_fit.html.

[96] M. Branch, T. F. Coleman, and Y. Li, A subspace, interior, and conjugate gradient method for large-scale bound-constrained minimization problems, SIAM J. Sci. Comput. **21**, 1 (1999).

[97] X. Xie, Y. Liu, Y. Yao, U. Schollwöck, C. Liu, and H. Ma, Time-dependent density matrix renormalization group quantum dynamics for realistic chemical systems, J. Chem. Phys. **151**, 224101 (2019).

[98] F. A. Y. N. Schröder, D. H. P. Turban, A. J. Musser, N. D. M. Hine, and A. W. Chin, Tensor network simulation of multi-environmental open quantum dynamics via machine learning and entanglement renormalisation, Nat. Commun. **10**, 1062 (2019).

[99] S. V. Dolgov, A tensor decomposition algorithm for large odes with conservation laws, Comput. Methods Appl. Math. **19**, 23 (2019).

[100] A. J. Dunnett and A. W. Chin, Efficient bond-adaptive approach for finite-temperature open quantum dynamics using the one-site time-dependent variational principle for matrix product states, Phys. Rev. B **104**, 214302 (2021).

[101] Y. Xu, Z. Xie, X. Xie, U. Schollwöck, and H. Ma, Stochastic adaptive single-site time-dependent variational principle, JACS Au **2**, 335 (2022).

[102] H. Wang and H.-D. Meyer, On regularizing the ML-MCTDH equations of motion, J. Chem. Phys. **149**, 044119 (2018).

[103] L. Chen, M. F. Gelin, Y. Zhao, and W. Domcke, Mapping of wave packet dynamics at conical intersections by time- and frequency-resolved fluorescence spectroscopy: A computational study, J. Phys. Chem. Lett. **10**, 5873 (2019).

[104] S. Mandal, F. Gatti, O. Bindech, R. Marquardt, and J. C. Tremblay, Stochastic multi-configuration time-dependent Hartree for dissipative quantum dynamics with strong intramolecular coupling, J. Chem. Phys. **157**, 144105 (2022).

[105] R. Orús, A practical introduction to tensor networks: Matrix product states and projected entangled pair states, Ann. Phys. (NY) **349**, 117 (2014).